

CHAPTER 3

Chapter 3

Issues of Atmospheric Correction, Data Redundancy and Image Classification

SUMMARY

While analyzing remote sensing data in order to derive meaningful interpretation, atmospheric correction and image classification form the two essential steps. However, when the data is hyperspectral data, one more step becomes essential and that is removal of redundant bands. Thus, this chapter comprises of the discussions regarding these three aspects. At the onset is the hyperspectral data analysis for atmospheric correction. The two kinds of techniques, namely-relative and absolute are discussed here in connection to their effect on vegetation assessment. As regards to data redundancy, feature extraction as well as reduction techniques are discussed. Their success is measured through the improvement in classification accuracy owed to them. Furthermore, due to very large number of bands conventional classifiers are not suitable, so hyperspectral-centric classifiers are discussed. This has led to the identification of the feature extraction/reduction method and classifier which yield the best classification accuracy while using hyperspectral data in various domains of vegetation assessment.

3.1 ISSUE OF ATMOSPHERIC INTERFERENCE

The solar radiation along the Sun-Sensor-Earth path undergoes absorption and scattering. The absorptions correspond to water vapor, oxygen, carbon dioxide etc. Amongst them, major atmospheric water vapor absorption bands are centered at approximately 940,1140,1380 and 1880 nm, oxygen absorption band at 762 nm and carbon dioxide absorption band near 2080 nm (Gao et al., 2009). As mentioned in chapter 1, accurate removal of atmospheric absorption and scattering effects is required. This process is called atmospheric correction which aims at converting radiance to reflectance. In quantitative analysis, it is almost mandatory to calculate reflectance but not so in qualitative analysis. Yet, the reflectance spectra being easy to understand and comprehend, it is a better choice. The same can be realized through the following figure 3.1.

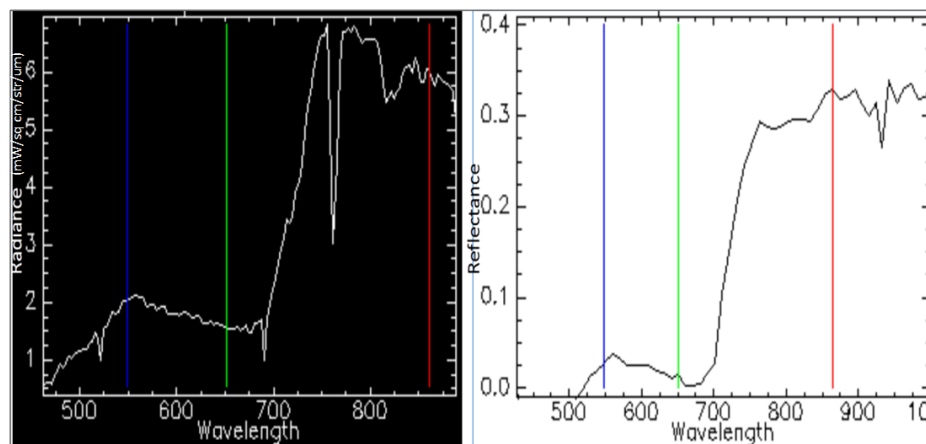


Figure 3.1: Radiance plot (Left) and Reflectance plot (Right) for vegetation

Radiance plot of vegetation in the above image shows a large number of prominent dips corresponding to atmospheric constituents. When these dips are flattened after

atmospheric correction, the reflectance image of the type shown in the above picture is generated. This resembles the spectra of vegetation. Thus, merely looking at the spectral profile, one can deduce the target under consideration and its status as well.

Now, atmospheric correction can be done through two methods -Relative or scene based empirical approaches and Absolute or radiative transfer modeling approaches. While relative methods do not give the actual reflectance but provide pseudo reflectance, absolute methods are more robust for they involve radiative transfer modeling. In quantitative analysis, the use of absolute methods is preferred but, can we use relative methods in hyperspectral data, is discussed in the following text.

3.1.1 Relative atmospheric correction techniques

During the mid-1980s, several scene-based empirical approaches were developed to remove atmospheric effects from hyperspectral imaging data for the derivation of relative surface reflectance spectra including flat field technique, Internal Average Relative Reflectance (IARR), Dark Object Subtraction (DOS) and log residuals. The kind of spectra these methods generate is discussed in the subsequent section.

3.1.1.1 Method

The atmosphere absorbs light very strongly in certain well-defined wavelengths. This causes image bands within those intervals to be relatively dark. The flat field correction technique is used to reduce this effect. Here, images, especially hyperspectral, are normalized in an area of known "flat" reflectance by assuming that there is an area in the scene that has spectrally neutral reflectance (Roberts et al., 1986). IARR (Kruse, 1988)

normalizes images to a scene average spectrum. This is particularly effective for reducing hyperspectral data to relative reflectance in an area where no ground measurements exist and little is known about the scene. The ‘Log Residuals’ remove solar irradiance, atmospheric transmittance, instrument gain, topographic effects and albedo effects from radiance data by creating a pseudo reflectance image. The logarithmic residuals of a dataset are defined as the input spectrum divided by the spectral geometric mean, then divided by the spatial geometric mean. It has a characteristic property of giving pronounced absorption at certain specific wavelengths. In DOS, atmospheric scattering corrections are applied to the image data. Here, the DN of the dark object in the image is subtracted from every pixel. This DN can be either the band minimum, an average based upon an ROI, or a specific value.

These methods were applied over HySI data and the resulting spectral profiles were studied.

3.1.1.2 Results and Discussions

For flat field correction, spectra of shallow (sand laden) water was used. It had spectrally neutral spectra. The whole image was then normalized. Consequently, spectra from vegetation pixels was, shown in figure 3.2. The resulting spectra looks like that of vegetation. The typical peak of chlorophyll absorption at 550nm is not observed, nonetheless, the inflexion point of red edge near 700nm exists along with the typical plateau like high reflectance in NIR region. The irregularities are reflected in each target spectrum where pseudo reflectance for vegetation goes beyond 1. *Thus, flat field correction may help in objectives like classification, where absolute atmospheric*

correction is not generally needed but not for quantitative studies like biochemical parameter estimation. This is in accordance with the results of Sourì and Sharifi (2012), who proved flat field to be effective in vegetation studies.

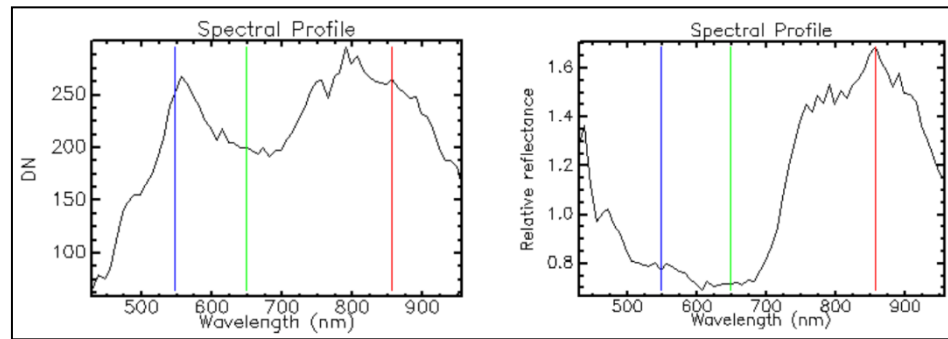


Figure 3.2: Vegetation spectra before (left) and after flat field correction (right)

When IARR was applied on the hyperspectral image, the plot of the type shown in figure 3.3 is generated. This method yields ‘vegetation like’ spectra, which is again the spectra of pseudo reflectance like that of flat field. However, two prominent dips are observed at 500nm and 700nm. The dip at 700nm can be explained as due to ‘red-edge’ but the 500nm dip is unexplainable. *Thus, here too, for objectives like classification, where absolute atmospheric correction is not generally needed, this method is of use.* Like flat field method, it is useful for vegetation studies.

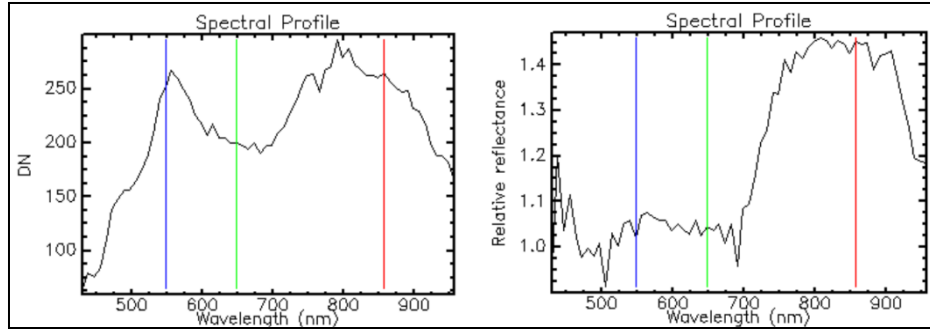


Figure 3.3: Vegetation spectra before (left) and after IARR (right)

In both the IARR and flat field approach, the derived relative reflectance spectra often have absorption features that are not present in reflectance spectra of actual materials (Clark & King, 1987). The reason is that the mean spectrum of the “flat field” is not 100% spectrally neutral or ‘flat’. The use of such spectrum can introduce broad absorption bands in the resulting spectra.

When the method of log residuals is applied, spectral plot of the type shown in figure 3.4 is obtained. The method gives ‘vegetation like’ spectra with prominent dips at places (like near 700nm) having little resemblance with actual materials. But, this dip is nearing ‘red edge’ region and hence emphasizes the presence of healthy green vegetation which shows sudden increase in NIR reflectance at red edge. Thus, it may be concluded here that *Log residuals stresses upon the important absorption features*. When compared to flat field and IARR, this method appears to have more saw-wave type noise. *Nonetheless, it may be used for classification purpose but not for quantitative assessments.*

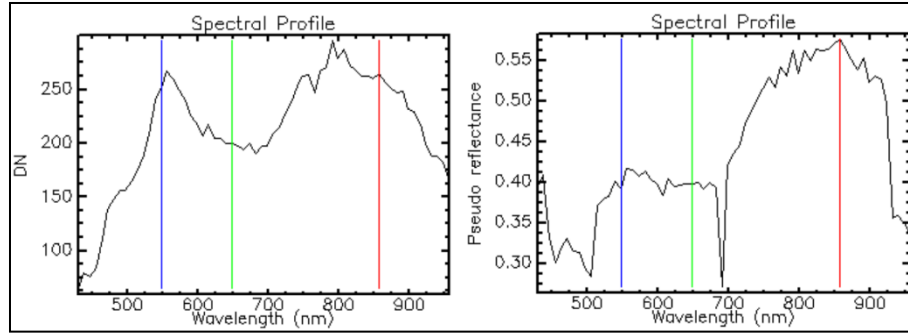


Figure 3.4: Vegetation spectra before (left) and after Log residuals correction (right)

For the application of DOS, two kinds of spectrally dark features were considered- band minimum and deep water. Figure 3.5 shows the results of Dark object subtraction (DOS) applied on the image. When DOS is done using band minimum for subtraction, the resultant spectra is just a variation of the input spectra and does not show any resemblance to typical vegetation spectral profile, although *it emphasizes upon the red-edge inflexion point*. When DOS involves subtraction using deep water DN, the typical vegetation spectral profile (pattern only) is observed. Gilmore et al. (2015) have proved the utility of DOS in discriminating wetlands using Landsat-8 data.

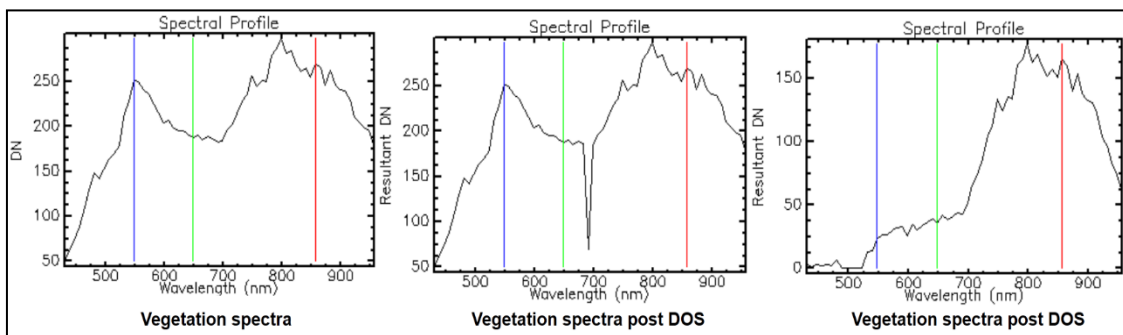


Figure 3.5: Vegetation spectra before DOS correction (left), after DOS correction using band minimum (center) and DOS correction (right)

As is clearly visible from the above figures, the selection of minimum value used to conduct DOS is crucial to arrive at the optimum results. The best selection is of dark dense vegetation, during its absence band minimum is preferred over deep water values.

3.1.2 Absolute methods

To compensate for atmospheric effects, properties such as the amount of water vapor, distribution of aerosols, and scene visibility must be known. Highly accurate models of atmospheric radiation transfer to produce an estimate of the true surface reflectance are then used. Atmospheric corrections of this type can be applied on a pixel-by-pixel basis because each pixel in a hyperspectral image contains an independent measurement of atmospheric water vapor absorption bands. The models under this category include ATREM (Gao and others, 1993), FLAASH (Matthew and others, 2000), ACORN (Miller, 2002), HATCH (Qu and others, 2003) and ATCOR (Richter, 1996). Here, FLAASH is studied for retrieving reflectance over vegetation using HySI data and AIMS data, collected at nadir view.

3.1.2.1 Method

Fast Line-of-sight Atmospheric Analysis of Spectral Hypercubes (FLAASH) is a first-principles atmospheric correction method developed for Hyperspectral Images for correction of visible through SWIR channels. It is based on MODerate resolution atmospheric TRANsmission code (MODTRAN-4) (Cooley et al., 2002). The important inputs include atmospheric models, water vapor retrieval band, aerosol model and

visibility range. Depending upon the average surface air temperature and water vapor, the type of the atmosphere is defined. In this case, Tropical model was selected which suffices to the conditions of mean surface air temperature as 27⁰C and mean water vapor as 4.11g/cm². To solve the radiative transfer equations that allow apparent surface reflectance to be computed, the column water vapor amount for each pixel in the image must be determined. For this water vapor absorption band at 1135 nm, 940 nm and for 820 nm can be used. As aerosols change with the change in the type of study area. Likewise, three kinds of aerosol models exist, Rural, Urban and Maritime. Thus, broadly, the choice of water vapor retrieval band and aerosol models may interfere with the retrieval of actual reflectance. To what extent they influence the spectral curve forms a part of this study. For this, three cases were considered-1) Without retrieving water vapor and aerosol, 2) Retrieving water vapor at 820nm but no aerosol and 3) retrieving both, water vapor and aerosol.

3.1.2.2 Results and Discussions

In the first case, water vapor channel was not defined. In that case, the water vapor was fixed at one value for the entire scene. Consequently, the reflectance image of HySI appears to be flattened, with little resemblance to the expected spectra (Figure 3.6). With the inclusion of water vapor retrieval at 820nm, the spectral plot bears little resemblance to the actual spectra, which gets further refined on retrieving aerosols. It may be noted here that still now the reflectance plot does not resemble the typical vegetation spectra. This is due to the quality issues discussed in last chapter.

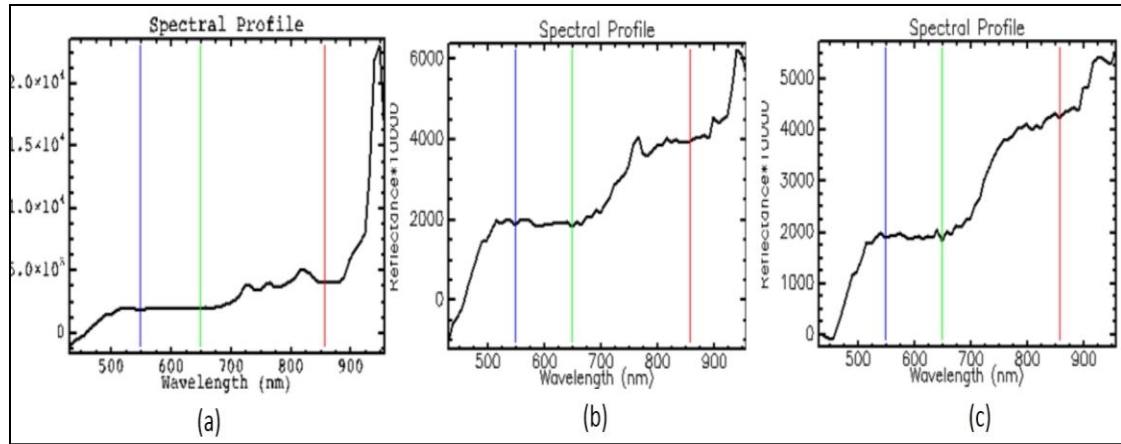


Figure 3.6: Reflectance images (a) Water vapor and aerosol not retrieved, (b) Water vapor retrieved at 820 nm but aerosol not retrieved, (c) Water vapor retrieved at 820 nm and aerosol retrieved

When the same kind of study was performed over AIMS data with basic corrections done, results of the kind shown in figure 3.7 are obtained. The range of wavelength is kept same in figures 3.6 and 3.7 so as to understand the ambiguity of the spectra in HySI image without correction. Here, variation of reflectance with different water absorption bands is studied. It is observed that using water vapor band is important but the wavelength region used out of the three mentioned above does not make much difference. However, in all the cases, the reflectance observed is higher than the standard reflectance (yellow line) obtained from Spectroradiometer observations in the NIR region and lower in the visible region. However, Rudjord and Trier (2012) showed that using FLAASH, reflectance in NIR region is less than the expected values but Kruse, 2014 supported the results discussed here.

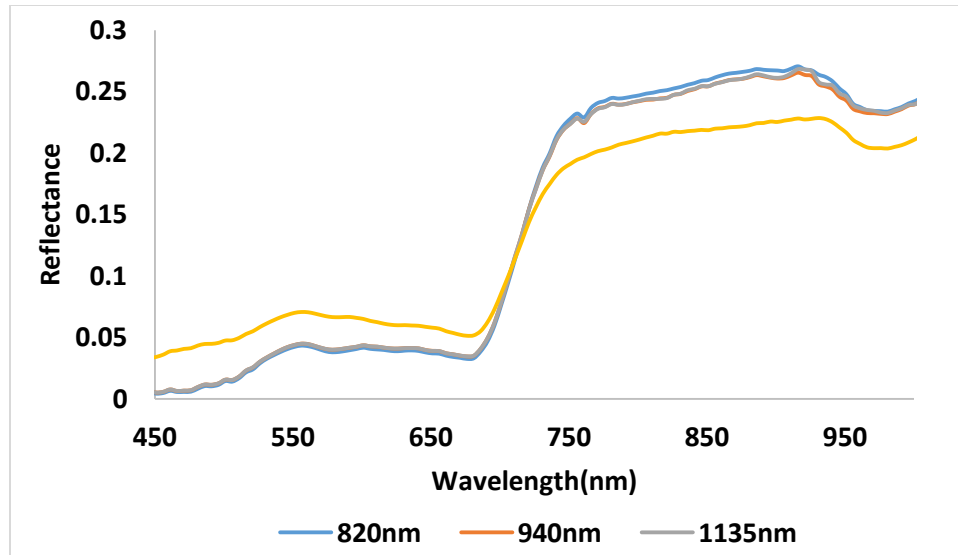


Figure 3.7: Reflectance image of spectra post application of FLAASH on AIMS data

Thus, it may be concluded that water vapor retrieval using one of the water vapor absorption channel is important in improving atmospheric correction.

When different methods for atmospheric correction are employed, namely FLAASH with atmosphere models Tropical and Mid-latitude summer; Empirical line method; 6S code and through Spectroradiometer observations, the variations in reflectance values are observed for vegetation. In figure 3.8, these methods are compared for three characteristic wavelengths of vegetation-red (NIR), green and blue, which are used for creating FCC.

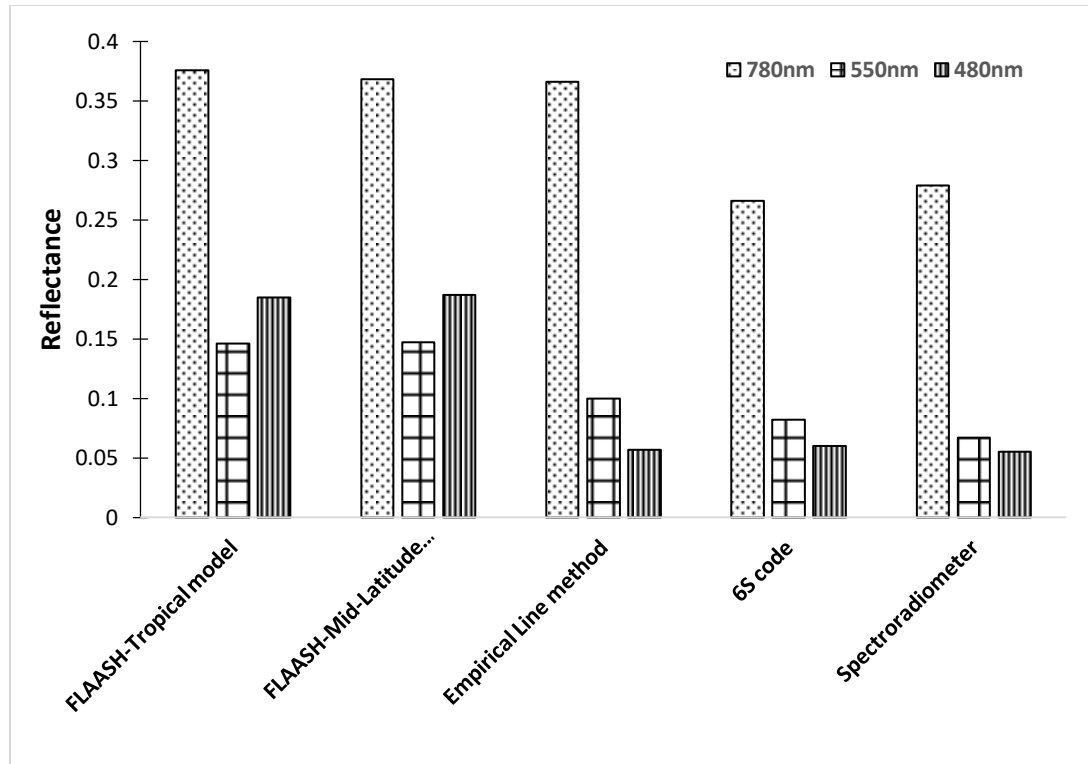


Figure 3.8: Comparison of reflectance values of vegetation obtained from various techniques for three bands used for creating FCC.

From the figure, it is clear that reflectance values obtained from Spectroradiometer and through 6S code match closely but vary significantly from both the absolute as well as relative methods of atmospheric correction. The use of either of the inbuilt atmospheric models in FLAASH doesn't affect the reflectance values greatly.

3.1.3 Other Factors

3.1.3.1 Effect of cross-track illumination

Airborne images are best acquired while the sensor platform is flying towards the sun as in that case the sun provides similar illumination conditions to all the targets captured in

the image (www.gege.fct.unesp.br). In practice, it is often not possible because of many reasons. The effect of varying azimuth angle and/or changing solar elevations occurs in terms of radiance. Visually too, it affects the image, as can be seen by figure 3.9.

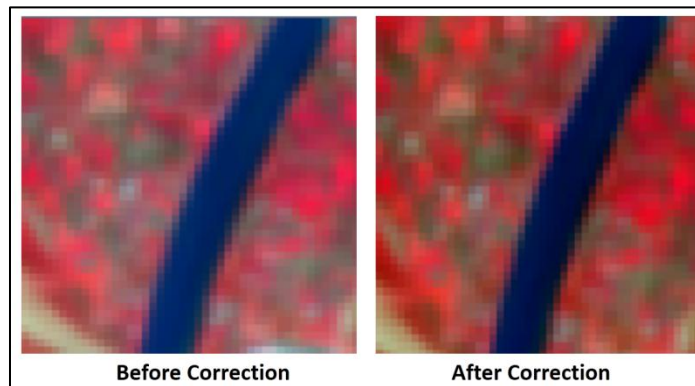


Figure 3.9: Image blurring on account of cross track illumination

3.1.3.2 Effect of change in zenith angle

Vegetation canopies are not lambertian reflectors and so their reflectance varies with sun and view angle change (Shibayama & Wiegand, 1985). Since, the nadir view is not always possible, so, impact of zenith angle variation on reflectance/radiance is important to know. The same holds true for Phytoplanktons. The surface radiance from the phytoplankton colonies changes with change in zenith angle. The same can be understood through figure 3.10. Here, with change in zenith angle from 0^0 to 90^0 , the surface radiance increases by 4-5 times. This calls for taking into account this effect before any inference is made from the data. The same kind of observation was shown by Xin et al (2012) for MODIS snow mapping in forests and also by Li et al. (2016).

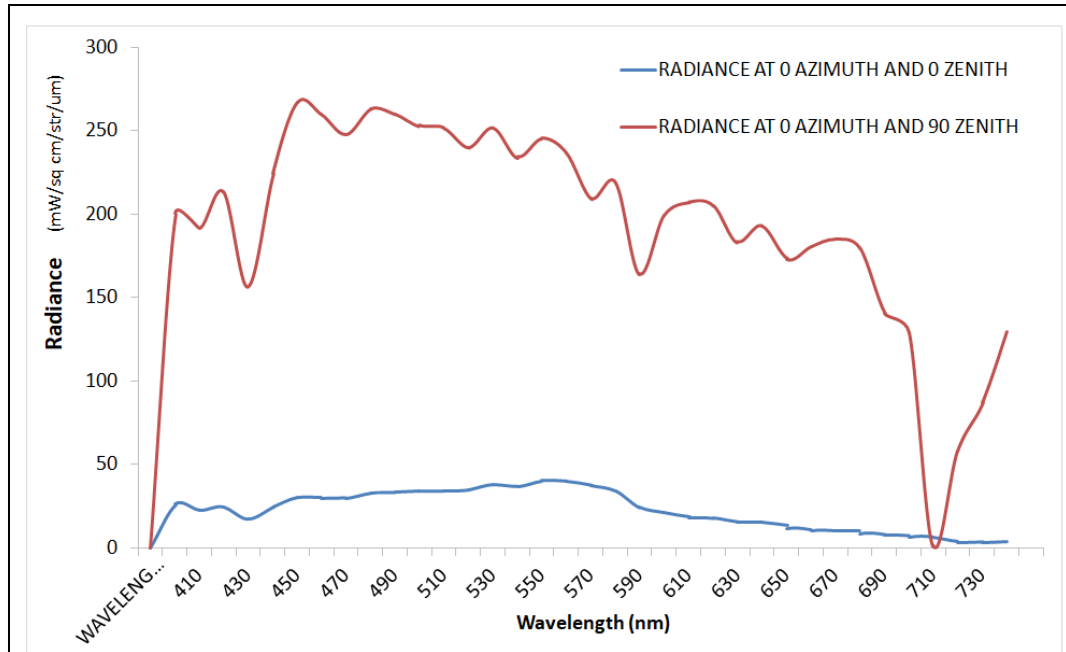


Figure 3.10: Effect of zenith angle change on surface radiance by Phytoplanktons with chlorophyll composition 10mg/m^3 , as simulated

3.2 DATA REDUNDANCY

Literature cites a number of dimensionality reduction techniques. The main being Step-wise Discriminant Analysis, Principal Component Analysis and Minimum Noise Fraction. These techniques are discussed here in terms of their role in utilizing hyperspectral data to its full potential. Additionally, a novel method of feature extraction based on image texture is also shown and discussed.

3.2.1 Method

Step-wise Discriminant Analysis (SDA)

The typical absorption features of any target correspond to the most important constituent of any target. Here comes the use of SDA which was performed through SPSS 16.0 software. It gives the best discriminating wavelengths using multivariate separability measures like Wilk's lambda, F value etc (Thenkabail, 2002). Wilk's lambda tests whether there are differences between the means of identified groups on a combination of dependent variables. Higher the value, less is the discrimination potential and vice versa as Wilk's lambda is an inverse measure (Chatfield and Collins, 1986). A combination of low Wilks' Lambda and high F-value shows higher discrimination and a zero value of Lambda indicated perfect separability. This method was implemented over Spectroradiometer observations of agricultural crops for discrimination of crop types, crop stage (Mango) and crop (Paddy) variety. Crop discrimination was based only on considering the trough locations but for Paddy varieties discrimination, the position of various absorption points as well as intensity of magnitude of the spectra were considered. This method was also implemented for discrimination of crop residue from standing matured crop and soil.

Principal Component Analysis (PCA)

For the Hyperion scene, random pixels in terms of regions of interest (ROIs) were taken on the radiance image and then were subjected to factor analysis so in order to identify underlying factors (bands) that explain the pattern of correlations. Principal components analysis (PCA) is a popular technique for data compression that produces uncorrelated bands, segregates noise and reduces dimensionality (Richards, 1999). The first

component has maximum variance. Successive components explain progressively smaller portions of the variance and are all uncorrelated with each other. The later components appear noisy because they contain very little variance, much of which is due to noise in the original spectral data (Richards and Jia, 2006). The technique adopted for rotation was Varimax method with Kaiser Normalization, which is an orthogonal rotation method that minimizes the number of variables that have high loadings on each factor (Norusis, 2004). This method simplifies the interpretation of the factors. Eigenvalues over one were only extracted and principal components were analyzed on the basis of correlation matrix. The selection of uncorrelated wavelengths was done using factor analysis tool in SPSS version 16.0. PC bands with large eigenvalues contain the largest amount of data variance, while bands with lower eigenvalues contain less data information and more noise.

Minimum Noise Fraction Based Dimensionality Reduction

Farrell et al (2005) suggested that for targeting at activities like discrimination of objects, PCA is not suitable. Nonetheless, Minimum Noise Fraction (MNF) transform, which essentially is noise adjusted PCA, is a better alternative. It is a two stage linear transform where noise is decorrelated and rescaled followed by PCA (Green, 1988). This method was implemented over Hyperion dataset.

Image Texture Based Dimensionality Reduction

Two basic categories of texture analysis can be defined, namely, statistical and structural. Statistical texture analysis techniques primarily describe texture of regions in an image

through higher-order moments of their grayscale histograms (Tomita and Tsuji, 1990). In simpler terms, it can be said that statistical approach sees an image texture as a quantitative measure of the arrangement of intensities in a region. On the other hand, structural texture analysis techniques describe texture as to comprise of well-defined texture elements. Texture analysis based on extracting various textural features from a gray level co-occurrence matrix (GLCM) (Haralick et al, 1973) is the most popular and cited technique. The GLCM approach is based on the use of second-order statistics of the grayscale image histograms. The GLCM functions characterize the texture of an image by calculating the co-occurrences of pixels with specific values in an image, creating a GLCM, and then extracting statistical measures from this matrix. The GLCM of an image is an estimate of the second-order joint probability, $P_{\delta}(i,j)$ of the intensity values of two pixels (i and j), a distance δ apart along a given direction θ . Haralick et al. (1973) proposed 14 textural parameters calculated from P_{δ} , all of which are seldom used. However, the correct choice of parameters lies in their ability to extract the most prominent features. For example, in areas with smooth texture, the range of values in the neighborhood around a pixel will be a small value; in areas of rough texture, the range will be larger. Similarly, calculating the standard deviation of pixels in a neighborhood can indicate the degree of variability of pixel values in that region. Here, GLCM based texture analysis was implemented over Hyperion dataset. This method includes ‘variance’, ‘homogeneity’ (Measures closeness of elements in GLCM to the diagonal elements), ‘contrast’ (Measures local variations), ‘dissimilarity’, ‘correlation’ (Measures joint probability) and ‘entropy’ (Degree of randomness) of the image in order to assess

the suitable bands for discrimination purpose. Table 3.1 describes methods of computation for the said texture parameters.

Table 3.1: Computation Formulae for Texture Parameters

Texture Parameter	Method of computation
Entropy	$S = -\sum_{i=1}^{to\ n} \sum_{j=1}^{to\ n} P_{\delta}(i,j) \log P_{\delta}(i,j)$
Contrast	$C = \sum_{k=0}^{to\ n-1} k^2 \sum_{i=1}^{to\ n} \sum_{j=1}^{to\ n} P_{\delta}(i,j)$
Correlation	$Co = (\sum_{i=1}^{to\ n} \sum_{j=1}^{to\ n} i \cdot j P_{\delta}(i,j) - \mu_x \mu_y) / \sigma_x \sigma_y$
Homogeneity	$H = \sum_{i=1}^{to\ n} \sum_{j=1}^{to\ n} P_{\delta}(i,j) / (1 + i-j)$
Variance	$(\sigma)^{1/2}$
Mean	$\mu_x = \sum_{i=1}^{to\ n} \sum_{j=1}^{to\ n} P_{\delta}(i,j)$ $\mu_y = \sum_{j=1}^{to\ n} \sum_{i=1}^{to\ n} P_{\delta}(i,j)$
Standard Deviation	$\sigma_x = \sum_{i=1}^{to\ n} (i - \mu_x)^2 \sum_{j=1}^{to\ n} P_{\delta}(i,j)$ $\sigma_y = \sum_{j=1}^{to\ n} (j - \mu_y)^2 \sum_{i=1}^{to\ n} P_{\delta}(i,j)$

In order to select the suitable bands for vegetation discrimination, the texture parameters, variance, homogeneity, contrast, dissimilarity, correlation and entropy were computed using GLCM. The GLCM matrix was created using each pixel along with its immediate horizontal neighbor (x shift=1 and y shift=0) for a 3*3-pixel window. Each texture parameter owned 196 images. Good quality bands (SNR>10) were selected for each texture parameter. This reduced the number of bands corresponding to each parameter. Finally, intersection of sets of bands was done to yield final number of reduced bands available for further analysis. Table 3.2 shows the permissible values for different texture parameters corresponding to SNR>10, above which the bands were removed. Outside the permissible values, the bands extracted played insignificant to poor roles in image

classification either by not affecting classification accuracy at all or by decreasing it by a few percentages. Also, each texture parameter was analyzed for its significance in modulating classification accuracy. This was done by deliberately removing one texture parameter at a time in the analysis to check the effect it imparts to the classification accuracy. Because, no significant contribution was shown by the parameters homogeneity and correlation in feature reduction by observing classification results, consequently, the same were dropped from further analysis.

Table 3.2: Texture parameters

S. No.	Texture parameter	Permissible value
1	Variance	>30
2	Homogeneity	Not suitable
3	Contrast	<10
4	Dissimilarity	>4
5	Entropy	>1
6	Correlation	Not suitable

3.2.2 Results and Discussions

Step-wise Discriminant Analysis

This method helps in identifying the spectral regions most suitable for discriminating a particular category. This is shown through discriminating agricultural crop types, agricultural crop varieties and stages and agricultural crop residue. The method is mostly applicable in cases where data is in non-image mode.

The performance of SDA is seen through its application for Paddy variety discrimination. Here, six varieties of paddy (paddy gr 4 to paddy gr 9) were studied. Figure 3.11 shows the spectral signatures of these varieties. It can be observed from the plot that all varieties

are distinguishable from each other but from visualization alone, it is not clear that which bands contribute the maximum in target discrimination. Thus, SDA was performed so as to find the best discriminating bands.

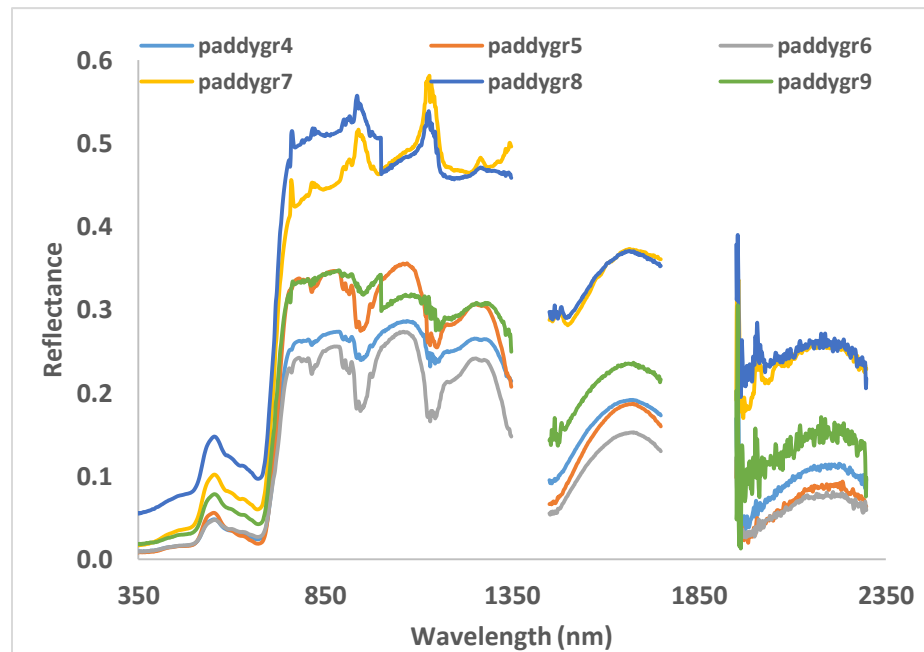


Figure 3.11: Spectral plots of paddy varieties

SDA yielded table 3.3 which shows the discriminating wavelengths, their Wilk's lambda as well as F value. Bands within the range of 646-686nm are mainly attributed to chlorophyll content. Hence, it is the quantitative difference in amount of chlorophyll content that remarkably differentiates the paddy varieties. Soil organic carbon and soil texture contribute mainly to the bands centered near 366nm, 416nm, 456nm and 1046nm. 966nm which corresponds to plant biochemical pigment concentration. Besides this, other bands, probably, are the outcome of the structural differences in the varieties of paddy. As a result, it can be said that with the hyperspectral set of bands appropriately

reduced through SDA, even minute discrimination between varieties of a particular crop can also be picked up.

Table 3.3: Step wise discriminant analysis results for Paddy variety discrimination

Wavelength	Wilk's lambda	F value
366	0.337	44.536
366, 686	0.043	86.128
366, 686, 646	0.028	54.055
366, 686, 646, 416	0.019	42.133
366, 686, 646, 416, 456	0.016	33.623
366, 686, 646, 416, 456, 1046	0.012	28.922
366, 686, 646, 416, 456, 1046, 2096	0.006	30.11
366, 686, 646, 416, 456, 1046, 2096, 1966	0.005	27.983
366, 686, 646, 416, 456, 1046, 2096, 1966, 766	0.004	26.357
366, 686, 646, 416, 456, 1046, 2096, 1966, 766, 966	0.003	25.097
366, 686, 416, 456, 1046, 2096, 1966, 766, 966	0.003	27.841
366, 686, 416, 456, 1046, 2096, 1966, 766, 966, 2186	0.002	26.207
366, 686, 416, 456, 1046, 1966, 766, 966, 2186, 2016	0.002	28.879

On similar grounds, the spectra of mango crop at three different stages- young, middle and mature ages was analyzed through SDA. The spectra are shown in Figure 3.12. Table 3.4, as an outcome of discriminant analysis, lists the bands suitable for discriminating the same.

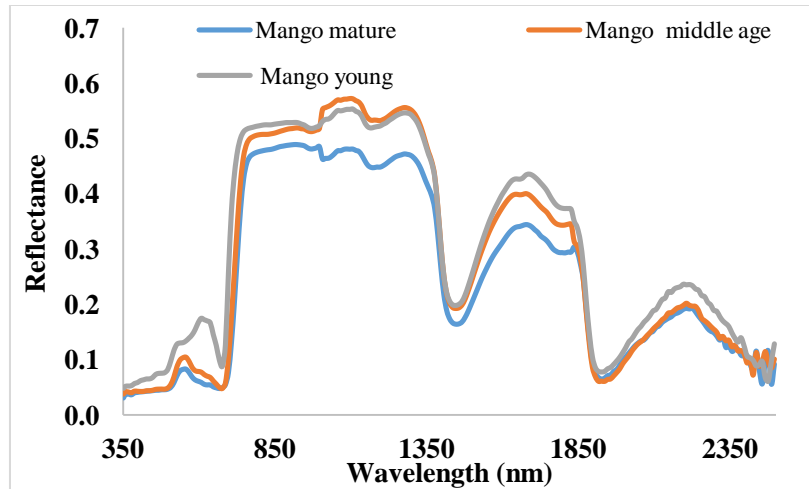


Figure 3.12: Spectral plots of three stages of Mango

Table 3.4: Results of Discriminant analysis for Mango stages

Wavelength (nm)	Wilks' Lambda	F-test
700	0.020	297.71
700,1010	0.002	129.48
420,700,1010	0.000	280.89
420,700,1010, 1970	0.000	316.44
420,700,1010, 1450,1970	0.000	606.58
420,700,1010, 1450,1970,2280	0.000	747.64
420,700,1010, 1450,1970,2110,2280	0.000	1080.54
420,700,1010, 1450,1970,2080, 2110,2280	0.000	1862.79

From the above figure, it may be observed that within the same species, age variation is clearly picked up by the spectra. This phenomenon is attributed to absorption features of Chlorophyll a and b in the blue region at around 430/450 nm and in the red domain at around 660/640 nm (Curran, 1990). The visible part of the vegetation reflectance spectrum is characterized by low reflectance values due to very strong absorption of the leaf pigments (Bertels et al., 2005). In mature leaves, reflectance in NIR region increases

as compared to young leaves because of increased leaf thickness. On the contrary, in far red region, opposite is observed owing to higher amount of photosynthetic pigments in young leaves. The same was observed by Gitelson et al. (2003).

Similarly, for discriminating the spectra of ten different agricultural crops, SDA was performed. The crops appear to be spectrally similar (Figure 3.13) but with marked differences in magnitude. However, there does exist some bands which are capable of discriminating various crops. Table 3.5, as an outcome of discriminant analysis, lists the bands suitable for discriminating the same.

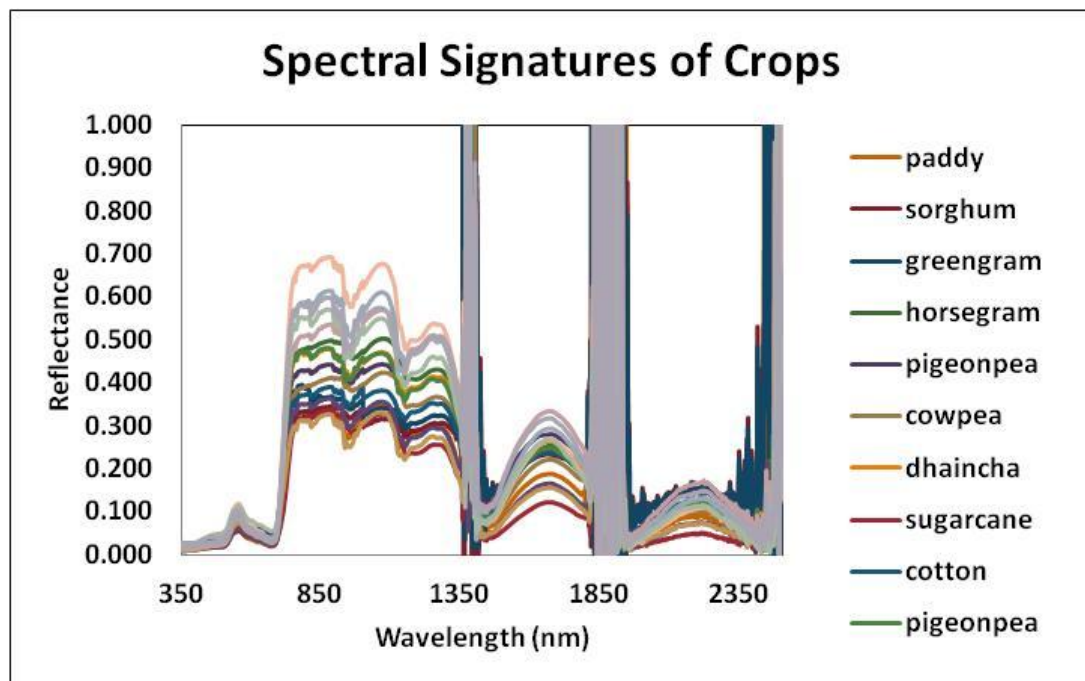


Figure 3.13: Spectral plots of spectrally similar crops

Table 3.5: Discriminating bands for various crops

Wavelength	Wilk's lambda	F value
1396	0.043	334.668
1396, 1636	0.011	126.371
1396, 1636, 1806	0.003	92.064
1396, 1636, 1806, 1136	0.001	79.914
1396, 1636, 1806, 1136, 1356	0	82.842
1636, 1806, 1136, 1356	0	132.166
1636, 1806, 1136, 1356, 1346	0	132.533
1636, 1806, 1136, 1356, 1346, 496	0	111.032
1636, 1806, 1136, 1356, 1346, 496, 616	0	100.917
1636, 1806, 1136, 1356, 1346, 496, 616, 706	0	97.56
1636, 1806, 1136, 1356, 1346, 496, 616, 706, 1176	0	91.793
1636, 1806, 1136, 1356, 1346, 496, 616, 706, 1176, 366	0	85.335
1636, 1806, 1136, 1356, 1346, 496, 616, 706, 1176, 366, 446	0	79.53
1636, 1806, 1136, 1356, 1346, 496, 616, 706, 1176, 366, 446, 2236	0	73.746
1636, 1806, 1136, 1356, 1346, 496, 616, 706, 1176, 366, 446, 2236, 516	0	69.226
1636, 1806, 1136, 1356, 1346, 496, 616, 706, 1176, 366, 446, 2236, 516, 1756	0	64.089

The discriminating bands near 1396 and 1636nm precisely correspond to the vegetation water content, 446 and 706nm correspond to the crop nitrogen content while 496nm to the crop biochemical pigments. Rest of the absorption bands either are attributed to soil texture/ composition or structural differences between crops.

Finally, SDA was employed for discriminating crop residue from other farm components.

The spectral curves of residue and different related land covers are shown in figure 3.14 where residue, straw and mature crop had absorption features in 2100nm region due to cellulose absorption, while soil has absorption features in 2200 nm due to clay-hydroxyl. It can be also observed that all the classes had mostly featureless curves in 400-1200 nm region. There is mainly magnitude difference in reflectance. Similar results were found in the Stepwise Discriminant Analysis. Ground based hyperspectral data collected for wheat crop residue was analyzed using the technique to select optimum bands for discrimination. In all, seven best bands (400, 990, 2200, 940, 1980, 2030, 2440 nm) were obtained suitable for discrimination between above mentioned targets (Table 3.6). Out of these seven bands, four were from the SWIR region. The bands 400, 990, 2440 nm got selected because of the magnitude difference in spectral reflectance of the four classes. The bands 1980, 2030 and 2200 nm got selected because of the typical absorption features, i.e. water, cellulose, clay-hydroxyl, respectively.

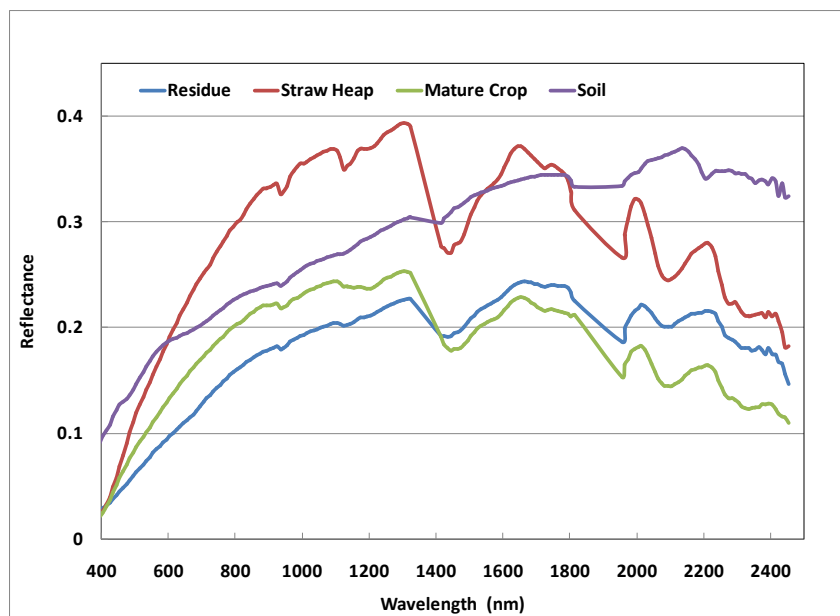


Figure 3.14: Average spectral plots of crop residue, matured crop, soil and straw heaps

Table 3.6: Stepwise Discriminant Analysis of different residue related classes

Wavelengths	Wilks' Lambda	F Value
400	0.036	327.1
400, 990	0.002	278.8
400,990, 2200	0.000	273.1
400,990, 2200, 940	0.000	272.1
400,990, 2200, 940, 1980	0.000	245.8
400,990, 2200, 940, 1980, 2030	0.000	238.3
400,990, 2200, 940, 1980, 2030	0.000	216.0

Thus, SDA is successful in discriminating crop species, variety, growth stage and residue. But, in all cases, Spectroradiometer observations were given as input. When the hyperspectral data comes in the form of image, apart from the high number of bands, the factors of noise etc. also dominate. In such cases, the methods which address these issues also are needed.

Principal Component Analysis and Minimum Noise Fraction

MNF is noise adjusted PCA. Application of PCA on Hyperion data lead to the development of scree plot of figure 3.15 showing Eigen value and Component number. The plot revealed that the inherent dimensionality of the data was two. The cumulative percentages of the components started at 97.10% for the first component. PC 1 alone contained maximum information (97.10%), followed by PC 2 (2.25%). With two PCs, more than 99% information had been captured.

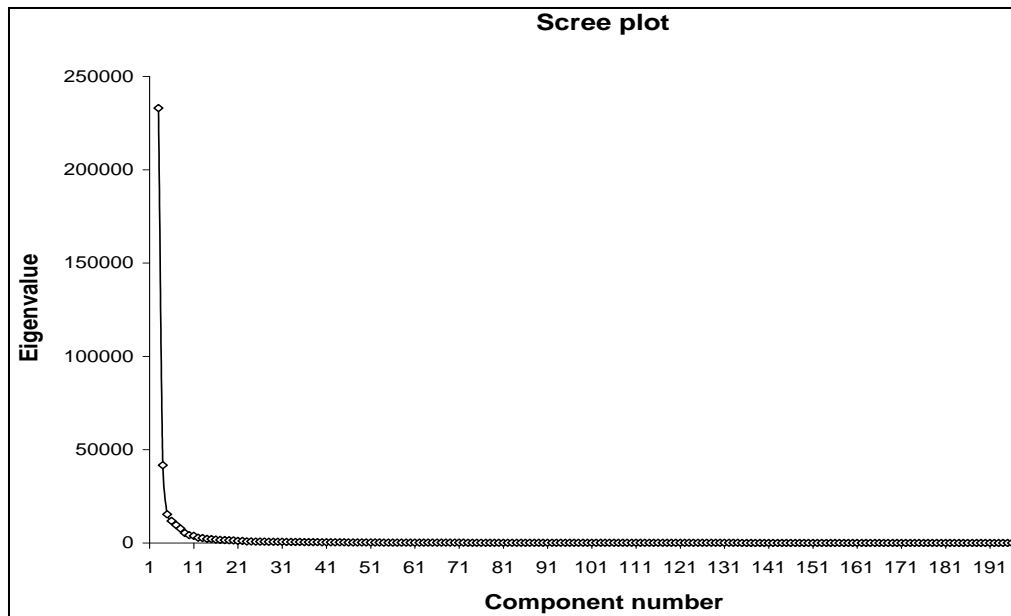


Figure 3.15: Cumulative percentages of the 196 principal components

Forward MNF transform was applied over Hyperion dataset. This yielded a large number of bands but with a constraint of Eigen value > 10 along with the simultaneous check on image noise, 6 MNF bands were obtained. These were the bands that were used for discrimination purpose.

Image Texture Based Dimensionality Reduction

The Image Texture Based Dimensionality Reduction reduced the number of bands. However, the different texture parameters ended up with different sets of bands. Hence, intersection of sets was performed to select the bands common to all parameters. Accordingly, out of 196 unique bands, best 56 bands were selected of which 22 fell in the range 427-630nm (Chlorophyll absorption region), 1 band centered at 681nm (Chlorophyll absorption region), 2 bands within 1073-1083nm, 7 bands between 1114 and 1185nm, 21 within 1457-1659nm (Lignin, cellulose and nitrogen absorption regions)

and 3 within 1861-1901nm. These bands were then adopted for further analysis i.e. classification. It is noteworthy that dominant absorption features are automatically selected through this procedure. Figure 3.16 shows the bands selected as a consequence of image texture analysis. It may be noted that frequency value 4 shows the common bands obtained through all the texture parameters collectively and hence the corresponding bands were selected.

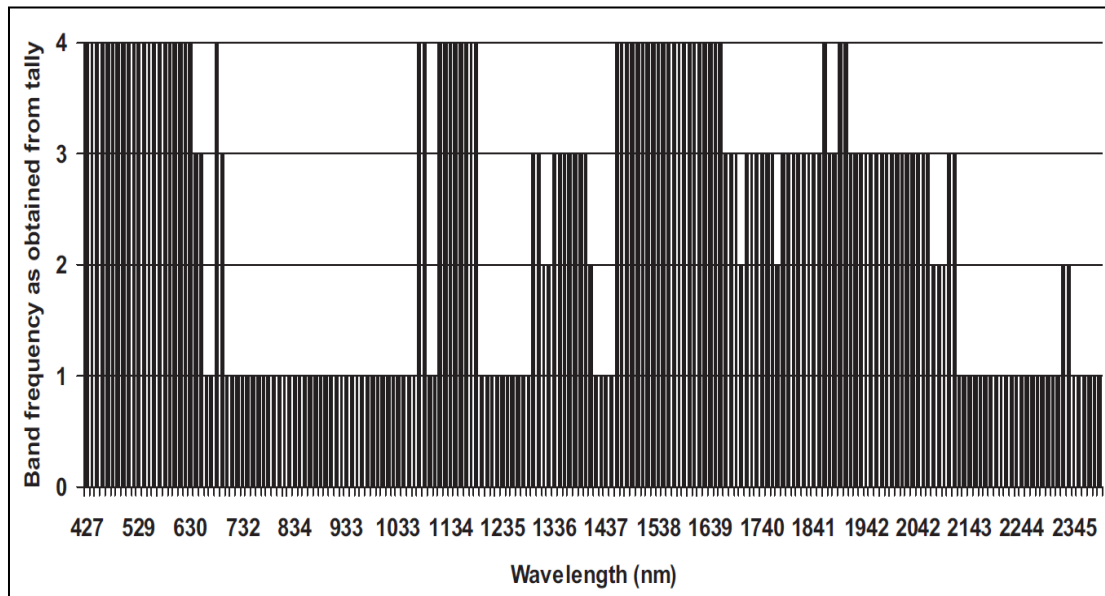


Figure 3.16: Bands selected after intersection of sets of bands corresponding to different texture measures

The effect of the above two techniques, namely image texture based feature extraction and MNF based dimensionality reduction, is observed through the results obtained after image classification in the following section.

3.3 IMAGE CLASSIFICATION

Supervised classification requires n^2-1 training sites (Hughes, 1968) where n is the number of bands. For broadband data this condition is easily met but not with hyperspectral data. Large number of bands in hyperspectral data pose serious limitations on selection of training sites (Hughes, 1968, Richards and Jia, 2006), classifier adopted and hence degrades classification accuracy. Consequently, the standard classifiers used for multi-spectral data are not suitable. Techniques specific to hyperspectral data like Spectral Angle Mapper (SAM) are the substitute. However, if features are appropriately selected/extracted, the richness of other classifiers can also be explored.

3.3.1 Method

Here, the dimensions obtained by using the two techniques (image texture based and MNF) were evaluated by comparing the classification results obtained from the use of various classifiers. Apart from the conventionally used Maximum likelihood, Minimum distance, Mahalanobis and Parallelepiped classifiers, the comparatively newer techniques like Support Vector Machine (SVM), Spectral Angle Mapper (SAM), Neural Network and Binary Encoding were also evaluated. In MD, Euclidean distance from each unidentified pixel to the mean vector for each class is computed. All pixels are classified to the nearest class unless a standard deviation or distance threshold is specified, in which case some pixels may be unclassified if they do not meet the selection criteria (Richards, 1999). SAM is a physically-based spectral classifier that utilizes an n -D angle to match pixels to reference spectra. The algorithm determines the spectral similarity between two spectra by calculating the angle between the spectra and treating them as vectors in a

space with dimensionality equal to the number of bands. SAM compares the angle between the endmember spectrum vector and each pixel vector in n-D space. Smaller angles represent closer matches to the reference spectrum. Pixels further away than the specified maximum angle threshold in radians are not classified (Kruse et al., 1993). SVM provides high-quality classification results from intricate and noisy data (Chang and Lin, 2001). It separates the classes with a decision surface that maximizes the margin between the classes. The surface is often called the optimal hyperplane, and the data points closest to the hyperplane are called support vectors. The support vectors are the critical elements of the training set (Wu et al., 2004). Binary encoding encodes the data and spectra into binary numbers, based on bands falling below or above the spectrum mean, respectively. An XOR function compares each encoded reference spectrum with the encoded data spectra and produces a classification image (Mazer et al, 1988). Here, these classifiers were evaluated for the different dimensionality reduction techniques. Supervised classification was performed by using the ground truth map of the study area. Confusion matrices were generated post classification.

Confusion Matrix

Once the image classification is done, post classification accuracy check is done. For this, confusion matrix with ground truth ROIs are used. The classes of all the classified images and the ROIs were matched to obtain the report on accuracy assessment. The report displays the overall accuracy, kappa coefficient (K), errors of commission, errors of omission, producer accuracy, and user accuracy for each class.

Jeffries-Matusita (J-M) distance analysis

For the quantification of spectral separability between various classes (obtained after image classification), separability index was used. It uses the square of Jeffries-Matusita (J-M) distance analysis. The J-M distance technique gives a value between 0 and $\sqrt{2}$. Value ≥ 1.90 indicates the separability of any two classes (Thomas et al., 2003). Because the J-M distance measure was a parametric scheme, it was necessary to decrease the number of spectral features (bands) prior to the calculation. In other words, it was not possible to calculate the J-M distance using all the selected (after data reduction) bands because of the singularity problem of matrix inversion.

3.3.2 Results and Discussions

Image classification of hyperspectral data was studied using Hyperion data at two sites- FRI, Dehradun and Bhitarkanika, Orissa

Study site-FRI, Dehradun

Post dimensionality reduction through image texture based approach and MNF, the resulting bands were subjected to classifiers. The classified output was then compared with the ground truth map of the study area and confusion matrix was generated. Table 3.7 shows a detailed comparison of different classifiers, in terms of accuracy (obtained through confusion matrix) when compared to ground truth map of the study area, vis-à-vis dimensionality reduction techniques.

Table 3.7: Evaluation of classifiers for dimensionality reduction through texture analysis and MNF transform

Classification Technique	Feature reduction through Texture analysis (Overall accuracy %)	Kappa coef.	Feature reduction through MNF transform (Overall accuracy %)	Kappa coef.
Binary Encoding	40.9	0.203	52.6	0.323
Minimum Distance	52.2	0.335	62.7	0.484
Neural Network	25.3	0.129	15.5	0
Parallelepiped	55.3	0.351	65	0.55
Spectral Angle Mapper	67.9	0.484	53.5	0.35
Support Vector Machine	82.73	0.67	64.7	0.507

It is clearly evident from table 3.7 that overall accuracy of classification is highest at 82.73% with SVM as classifier and feature reduction through image texture analysis. However, with MNF transform, maximum accuracy is yielded by Parallelepiped classifier (65%). Figure 3.17 shows the classified image using SVM classifier and image texture based feature reduction. *Thus, combination of SVM classifier and image texture based dimensionality reduction outperforms all other combinations.*

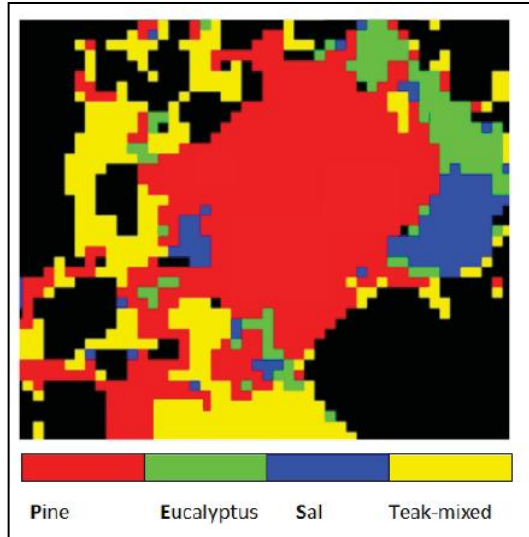


Figure 3.17: Classified scene of the study area using image texture based dimensionality extraction and SVM as classifier

Study site- Bhitarkanika Mangrove forests

When the same methodology of image classification (SAM, SVM, and MD) was implemented for Hyperion, Bhitarkanika, figure 3.18 is obtained. Post classification accuracy revealed that SVM was a better classifier, as was in previous case study [bands taken = 196, overall accuracy = 97.97%, Kappa coefficient (K) = 0.97)] than either MD (75.28%, 0.69) or SAM (65.39%, 0.59). Apart from 196 bands, the image was also subjected to SVM classification using 148, 98, 88, 76, 63, 39, 23 and 8 bands. The decrease in classification accuracy was insignificant for 148 bands (0.89%), remained the same for 98/ 88/ 76/ 63/ 56 bands (1.12%), again decreased slightly for 39 bands (1.57%), and significantly decreased for 23 and 8 bands. Based on these results, between 98, 56 and 39 number of bands, the selection was made for 56 bands. This is because 98

bands would have added redundancy while 39 bands were avoided to prevent further loss of information.

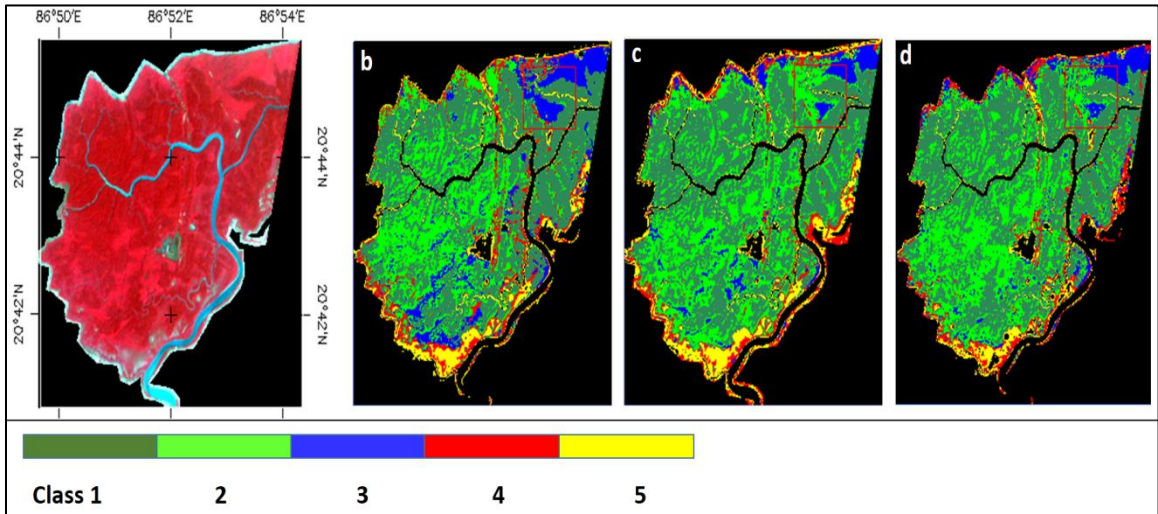


Figure 3.18: a) FCC of the image; b) SAM classified, c) MD classified and d) SVM classified images

Class 1 of the SVM classified image represented dense and dominant community of *Heritiera fomes*. Class 2,3 and 4 represent mixed mangroves in various combinations Mangrove associates and salt tolerant grasses were denoted by Class 5. The classification accuracy for these classifiers is shown in table 3.8

Table 3.8: Accuracy of Hyperion classified images

Classifier	Support Vector Machine	Minimum Distance	Spectral Angle Mapper
Overall accuracy (%)	96.85	72.81	70.11
Kappa coefficient K	0.96	0.66	0.64

Post classification, the optimal Wilks' Lambda was achieved with four bands for discriminating the five mangrove classes ($L = 0.000$, F-value = 29.19) (Table 3.9). The pair-wise spectral separability in terms of J-M distance was calculated using the 4 bands of table 3.9 and is shown in table 3.10. The results of the table revealed that the overall spectral separability between the pairs of the mangrove classes was high, since most of them acquired levels of separability much higher than the selected threshold of 0.9.

Table 3.9: Selected bands, Wilks' lambda and F statistics from SDA

Step	Wavelength(s) in nm	Wilks' lambda	F value
1	630.32	0.336	4.93
2	630.32, 2193.73	0.010	20.55
3	630.32, 1063.79, 2193.73	0.001	28.28
4	630.32, 983.08, 1063.79, 2193.73	0.000	29.19

Table 3.10: The J-M distances between the pairs of mangrove classes

Class	1	2	3	4	5
1	-				
2	1.99				
3	2.00	1.99			
4	1.98	1.99	1.99		
5	1.99	2.00	2.00	1.98	-

From both the case studies, it may be concluded that SVM classifies vegetation better when species level discrimination is required.

References

- Bertels, L., Bart, D., Pieter, K., Provoost, s., Tortelboom, E. (2005). Potentials of airborne hyperspectral remote sensing for vegetation mapping of spatially heterogeneous dynamic dunes, a case study along the Belgian coastline. Proceedings 'Dunes and Estuaries 2005' – International Conference on Nature Restoration, 153-163.
- Chang, C.C., Lin, C.J. (2001). LIBSVM: A Library for Support Vector Machines.
- Chatfield, C. and Collins, A.J. (1986). Introduction to multivariate analysis (revised edition). Chapman and Hall, London.
- Clark, R.N. and King, T.V.V. (1987). Causes of spurious features in spectral reflectance data. In Proc. of the third airborne imaging spectrometer data analysis workshop (G Vane, Ed) JPL Publications Jet Propulsion lab, Pasadena, CA, pp 132-137
- Cooley, T., Anderson, G.P., Felde, G.W., and others. (2002). FLAASH, a MODTRAN-4 based atmospheric correction algorithm, its application and validation. IEEE international geoscience and remote sensing symposium, DOI 10.1109/IGARSS.2002.1026134
- Curran, P.J., Dungan, J.L., Macler, B.A., Plummer, S.E. (1990). The effect of a red leaf pigment on the relationship between red-edge and chlorophyll concentration. Remote Sensing of Environment. 35, 69–75.
- Farrel, M.D., and Mersereau, R.M. (2005). On the impact of PCA dimension reduction for hyperspectral detection of difficult targets. IEEE geoscience and remote sensing letters, 2 (2), 192-195
- Gao, B.C., Heidebrecht, K.B. and Goetz, A.F.H. (1993). Derivation of scaled surface reflectances from AVIRIS data. Remote Sensing of Environment. 44(2-3), 165-178. doi:10.1016/0034-4257(93)90014-O
- Gao, B.C., Montes, M.J., Davis, C.O., Goetz, A.F.H. (2009) Atmospheric correction algorithms for hyperspectral remote sensing data over land and ocean. Remote Sensing of Environment. 113: 517-524.

- Gilmore, S., Saleem, A., Dewan, A., Effectiveness of DOS (Dark-Object Subtraction) method and water index techniques to map wetlands in a rapidly urbanizing megacity with Landsat 8 data In: B. Veenendaal and A. Kealy (Eds.): Research@Locate'15, Brisbane, Australia, published at <http://ceur-ws.org>.
- Gitelson, A.A, Gritz, Y., Merzlyak, M.N. (2003). Relationships between leaf chlorophyll content and spectral reflectance and algorithms for non-destructive chlorophyll assessment in higher plant leaves. *Journal of Plant Physiology* 160, 271–282.
- Green, A.A., Berman, M., Switzer, P. and Craig, M.D. (1988). A transformation for ordering multispectral data in terms of image quality with implications for noise removal. *IEEE transactions on geoscience and RS*. 26(1). p 65-74.
- Haralick, R.M., Shanmugam, K. and Dinstein, I. (1973). *IEEE Trans. Syst. Man Cybern.* **3**. pp. 610–621.
- Hughes, G.F. (1968). On the mean accuracy of statistical pattern recognizers. *IEEE Transac. On Info. Theory*, 14, 55-63.
- <http://gege.fct.unesp.br/docentes/cartoenner/PPGCC/Hiperespectral/Lab%20%2020%20Image%20preprocessing/session%2004%20Cross%20track%20illumination%20correction.pdf>
- Kruse, F.A. (1988). Use of airborne imaging spectrometer data to map minerals associated with hydrothermally altered rocks in the Northern Grapevine Mountains, Nevada and California. *Remote Sensing of Environment* 24: pp 31-51.
- Kruse, F.A. (2014). Comparison of ATRME, ACORN and FLAASH atmospheric correction using low altitude AVIRIS data of Boulder, CO, <https://www.researchgate.net/publication/228699945>
- Kruse, F.A., Lefkoff, A.B., Boardman, J.B., Heidebrecht, K.B., Shapiro, A.T., Barloon, P.J., Goetz, A.F.H. (1993). The Spectral Image Processing System (SIPS) - interactive visualization and analysis of Imaging spectrometer data. *Remote Sensing of the Environment* 44: 145 - 163.

- Li, H., Li, X. and Xiao, P. (2016). Impact of Sensor Zenith Angle on MOD10A1 Data - Reliability and Modification of Snow Cover Data for the Tarim River Basin. *Remote Sens.* 8, p 750, doi:10.3390/rs8090750
- Matthew, M. W., Adler-Golden, S. M., Berk and others. (2000). Status of Atmospheric Correction Using a MODTRAN4-based Algorithm. *SPIE Proceedings, Algorithms for Multispectral, Hyperspectral, and Ultraspectral Imagery 4049*, pp. 199-207
- Mazer, A. S., Martin, M., Lee, M., and Solomon, J. E.. (1988). Image Processing Software for Imaging Spectrometry Analysis. *Remote Sensing of the Environment.* 24(1), p. 201-210.
- Miller, C.J. (2002). Performance assessment of CORN atmospheric correction algorithm. *Proceedings of SPIE, V-4725*, p 438-449
- Norusis, M. (2004). *SPSS 12.0 Guide to Data Analysis*. Prentice-Hall, Inc. Upper Saddle River, NJ, USA, ISBN:0131478869
- Qu, Z., Kindel, B.C. and Goetz, A.F.H. (2003). The high accuracy atmospheric correction for hyperspectral data (HATCH) model. *IEEE Transactions on Geoscience and Remote Sensing*, 41(6/1), 1223–1231. doi:10.1109/TGRS.2003.813125
- Richards, J.A.(1999). *Remote Sensing Digital Image Analysis: An Introduction*, Springer-Verlag, Berlin, Germany p. 240.
- Richards, J.A., Jia, X. (2006). *Remote Sensing Digital Image Analysis: An Introduction*, 4th edition. Springer, Germany
- Richter, R. (1996) Atmospheric correction of satellite data with haze removal including a haze/clear transition region. *Computers and Geosciences.* 22(6), 675–681. doi:10.1016/0098-3004(96)00010-6
- Roberts, D.A., Yamaguchi, Y. and Lyon, R.J.P. (1986). Comparison of various techniques for calibration of AIS data: in proceedings, 2nd AIS workshop, JPL Publications, 86-35, Jet Propulsion Laboratory, Pasadena, CA, P 21-30

- Rudjord, O. and Trier, O. D. (2012). Evaluation of FLAASH atmospheric correction, NR_notat SAMBA/10/12, pp 24.
- Shibayama, M. and Wiegand, C.L. (1985). View azimuth and zenith, and solar angle effects on wheat canopy reflectance. *Remote Sensing of Environment*. 18 (1), pp 91-103
- Souri, A.H., Sharifi, M.A. (2012). Evaluation of Scene-Based Empirical Approaches for Atmospheric Correction of Hyperspectral Imagery, The 33rd Asian conference on remote sensing Nov 26-30.
- Thenkabail, P.S., Smith, R.B., De Pauw E. (2002). Evaluation of narrowband and broadband vegetation indices for determining optimal hyperspectral wavebands for agricultural crop characterization. *Photogrammetric Engineering and Remote Sensing*. 68,607–621
- Thomas, V., Treitz, P., Jelinski, D., Miller, J., Lafleur, P., Mccaughey, J.H. (2003). Image classification of a northern peat land complex using spectral and plant community data. *Remote Sensing of Environment* 84: 83–99.
- Tomita, F. and Tsuji, S. (1990). *Computer analysis of visual textures*. Kluwer Academic Publishing, Massachusetts.
- Wu, P. and Thomas G. (2004). Improving SVM Accuracy by Training on Auxiliary Data. <http://web.engr.oregonstate.edu/~tgd/publications/ml2004-auxiliary-data-for-svms.pdf>
- Xin, Q., Curtis, E. W., Liu, J., Tan, B., Melloh, R.A., Davis, R.E. (2012). View angle effects on MODIS snow mapping in forests. *Remote Sensing of Environment*. 118, pp 50–59, doi: 10.1016/j.rse.2011.10.029.